Subsurface structural delineation and mineralisation potential from integration of aeromagnetic and remote sensing datasets in Gabal Abu Rahaya area, South Eastern Desert, Egypt

Sayed Omar ELKHATEEB[1], Ahmed M. ELDOSOUKY[2,*] (iD),
Basma Mohammed HEBASHI[1]

[1] Geology Department, Faculty of Science, South Valley University, 83523, Qena, Egypt

[2] Department of Geology, Faculty of Science, Suez University, P.O. Box 43221, Suez, Egypt

Abstract: This study investigates the subsurface geological structures and mineralisation zones in the Gabal Abu Rahaya area, South Eastern Desert, Egypt, using integrated geological, remote sensing, and aeromagnetic data. Landsat-8 imagery was processed to identify lithological contacts and fault zones, creating a refined geological map of the region. Aeromagnetic data were analysed using geophysical filters such as Reduced-to-Pole (RTP), Tilt Derivative (TDR), Centre for Exploration Targeting (CET) porphyry analysis, and Euler deconvolution to delineate subsurface structural features and mineralisation patterns. The results from both remote sensing and magnetic data showed consistent structural trends, including matching fault and contact zones, which significantly improved the reliability of structural interpretations. This data integration enhances the delineation of prospective mineralised zones, making it possible to refine geological models for the area. The approach successfully combines satellite imagery and aeromagnetic data, offering a useful methodology for mineral exploration in complex, poorly mapped regions. Ultimately, the study provides a model for targeting ore deposits in similar geologically challenging terrains, contributing to more accurate mineral exploration.

Key words: aeromagnetic, remote sensing, Egypt, South Eastern Desert, mineralisation, edge detection

1. Introduction

Gabal Abu Rahaya area is positioned in the Eastern Desert of southern Egypt. Despite being surrounded by numerous promising gold discoveries, there haven't been many discoveries in the field itself. This might be attributed to the dearth of thorough geomorphological mapping and the small

---

*corresponding author, e-mail: Ahmed.Eldosouky@sci.suezuni.edu.eg

number of thorough geological surveys. Furthermore, because of their closeness to cities and their lengthy mining and exploration history, which dates back to the Pharaonic era, the northern (NED) and central (CED) sections of the Eastern Desert have drawn a lot of scholarly interest. The southern Eastern Desert (SED), in contrast, has received less attention, underscoring the need for further data and study to fully comprehend its geological makeup and salient features.

Although there may be some parallels between the SED and the CED's geological structure, research implies, it contains older rock formations and has undergone more complex geological transformations, with less influence from the major Najd shear system, and also is characterized by the existence of the pre- Pan-African rocks of the medium-grade gneiss, which include continental shelf sediments intruded with alkali granitoids. These rocks are exposed underneath ophiolitic belt that is encompassed between the NW–SE trending orogenic belts (*O'Conner et al., 1994*).

Because of these geological obstacles, it is challenging to precisely define mineralised zones, which create uncertainty in ore deposit, mine design, mineral exploration, evaluation, and resource extraction. According to *Haldar (2018)*, mineral exploration focuses on activities that are interested in finding new minerals and assessing profitable ones. An efficient method for identifying subsurface objects and desirable drilling locations is the geophysical survey (*Haldar, 2018*). Magnetic methods are considered one of the common beneficial accessible tools that assist in the identification of the surface and subsurface geology. The goal of the utilization of the aeromagnetic analysis is to help in explaining the problems of provincial geologic mapping and structure (*Eldosouky, 2019; Sehsah et al., 2019; Eldosouky and Mohamed, 2021; Melouah and Pham, 2021*). *Eldosouky et al. (2017, 2020, 2021)* and *Ekwok et al. (2019)* used aeromagnetic and remote sensing data to discuss mineralisation, density of sedimentary cover, representation of buried contacts, and the location of the presumed fields of rock differentiation.

Geological studies have been carried out in the vicinity of Gabal Abu Rahaya area by several researchers, including *Abdelsalam and Stern (1996)*, *El-Shimi (2005)*, and *Elkhateeb and Eldosouky (2016)*, who assessed the Wadi Allaqi region's potential for mineralisation using aeromagnetic analysis. Geological investigations have shown a sedimentary layer of around

2,300 metres in thickness in the region's stratigraphy, including results from the El-Nom borehole in the Gebel Abraq region southeast of Aswan (*Mahmoud and Essa, 2007*). This sequence, which spans geological eras from the Berriasian to the Cenomanian, is mostly composed of siltstone, black shale, fine-grained quartz-rich sandstone, and cemented sandstone.

Aeromagnetic surveys are utilized frequently in mineral exploration as they provide detailed maps of variations in rock magnetization, making them a valuable tool to point out subsurface geological structures. Using sophisticated methods like reduction to the pole (RTP) and adding filters like tilt angle analysis, CET porphyry and Euler Deconvolution on aeromagnetic data researchers can increase the precision of geological and structural mapping and identify possible mineralised regions. Because they frequently signal the presence of economically viable mineral deposits, hydrothermal alteration districts are primarily important in mineral prospecting (*Eldosouky et al., 2017, 2020, 2021*).

To effectively identify mineral-rich sectors as well as hydrothermal alteration zones, tools such as principal component analysis (PCA) and band ratio analysis are used to investigate hydrothermal alteration and distinguish lithological units in various contexts across the world (*Banerjee et al., 2019; Zoheir et al., 2019c; Elsayed Zeinelabdein et al., 2020; Howari et al., 2020; Sekandari et al., 2022; Abd El-Wahed et al., 2021; Pour et al., 2021*).

Furthermore, several microwave sensor items are more advantageous and efficient for mapping structural features and deformational settings (*Kusky and Ramadan, 2002; Pour and Hashim, 2015a; 2015b; Pour et al., 2016; 2018; Khalifa et al., 2021*).

Mineral exploration in the upper crust benefits greatly from the integration of many geophysical, remote sensing, and structural datasets (*Chen et al., 2004; Eldosouky et al., 2021, 2024; Aali et al., 2022; Kharbish et al., 2022; Mahdi et al., 2022; Maleki et al., 2022*).

Therefore, geological mapping and mineral exploration in the Gabal Abu Rahaya area can be significantly enhanced by combining data from remote sensing with the findings of aeromagnetic surveys.

This combination strategy increases the likelihood of finding new mineral deposits in the southern Eastern Desert, which is currently understudied. Particularly in polymetallic and very worn basement areas, where the integration of remote sensing, geophysical, structural, and geological

data using artificial intelligence produces beneficial results (*Bencharef et al., 2022*).

The main goal of this study is to find the best locations for mineralisation and hydrothermal zones based on the identification of surface and subsurface structures using the combination of remote sensing images and aeromagnetic data. This will also make it easier to identify the various lithologic units and point out potential mineralisation zones.

2. Location and geology

According to *Zoheir et al. (2019b); Stern (1994)*, economically important minerals including gold, copper, and iron are abundant in the Egyptian Eastern Desert (EED), especially in its central and southern regions. Therefore, the SED has undergone extensive mineralogical and geological investigations by several researchers (*Akaad and El-Ramly, 1960; Abdel-Karim, 2021; Kusky and Ramadan, 2002; Zoheir et al., 2018*). The region is located east of Aswan between longitudes $33°\,37'$ & $34°\,22'$ E and $23°\,02'$ & $23°\,23'$ N (Fig. 1a). It covers approximately 2400 km^2.

Because there hasn't been much geological research done in the area under investigation, we used previous studies on the SED generally and its adjacent areas specifically to describe the lithologic units in the Gabal Abu Rahaya area. *Conoco (1987)* provided the geological map for the area under study, which is characterized by an extremely arid environment where rainfall is scarce, and mainly covered by foreland sediments which are represented by Cretaceous Nubian Sandstones and Quaternary deposits. The sedimentary cover is underlain by Precambrian rocks which are mainly younger granites (Fig. 1b). The Nubian Sandstones are unconformably overlying the basement rocks and can be classified into three units corresponding to the lithological and photogeological characteristics (*El Tarras, 1995*).

The exposed basement rocks include metamorphic and igneous units covering the south-eastern, north-western, and southwestern parts of the study area. The metamorphic rocks include the oldest deformed rock units in the area. The exposed igneous rocks in the study area are mostly of granitoid composition. These rocks and the hydrothermal deposits are the focus of this study. The sedimentary cover in the north-eastern part of the study area revealed the dominance of Upper Cretaceous Nubia sandstone succes-
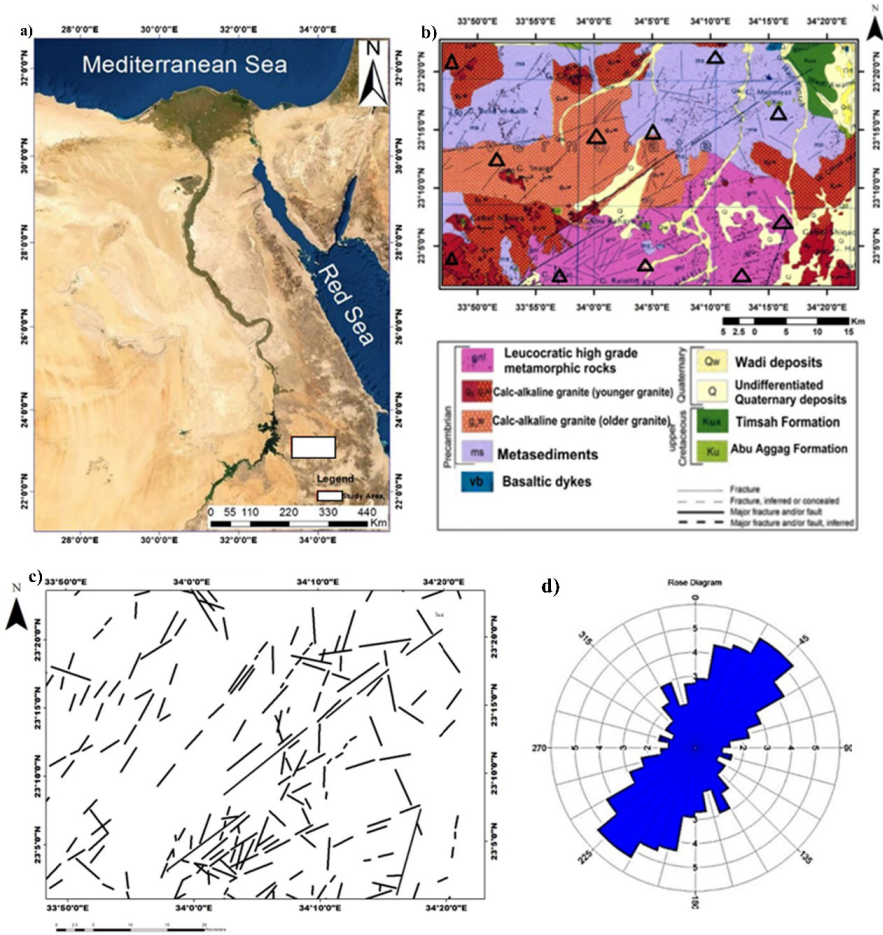
Fig. 1. a) Location map of the study area; b) geologic map of the Gabal Abu Rahaya area (*Conoco, 1987*); c) rose diagram of the surface structures that affected the study area; and d) rose diagram of the surface structures that affected the study area.

sion which is arranged from oldest to youngest as follows; Abu Aggag and Um Barmil formations overlain by Quaternary represented by alluvial deposits covering the distributed wadies in the study area.

The extracted structural lineaments from the geologic map in Fig. 1b shows that the study area is affected by surface faults trending in the N, NE–SW, ENE–WSW, NW–SE, and WNW–ESE directions (Figs. 1c, 1d).

3. Material and methods

3.1. Remote sensing data

The detection of hydrothermal mineralisation, as well as the spatial distribution and expansion of their fluid routes, are the main topics of this investigation. Therefore, the remote sensing (RS) datasets selected to accomplish this aim, and the primary source of lithological mapping for the studied region, are Landsat-8. The data can be easily downloaded from the online linkages (`http://earthexplorer.usgs.gov` and `http://glovis.usgs.gov`). To achieve accurate surface reflectance for precision processing, atmospheric corrections were performed using the FLAASH module in ENVI v.5.1 on Landsat-8 images.

Since the area of interest is smaller than the Landsat 8 OLI scene, the undesirable portions were cropped using a subset function, leaving just the area needed for analysis. This method reduces the amount of data stored on the computer's hard disk while simplifying and expediting additional processing.

Band ratioing is a simple yet effective technique in remote sensing. *Weissbrod et al. (1988), Cappiccioni et al. (2003)*, and *Gerck and Hurtak (1992)* employed this technique to extract spectrum information from multi-spectral data. Its foundation lies in emphasizing the spectral variations specific to the materials being mapped. It works by dividing the Digital Number (DN) values of one band by those of another, producing a grayscale image that reflects relative band intensities (*Sabins, 1997*).

In mineral prospecting, band ratio is commonly used to improve the spectral characteristics of the alteration zones based on the absorption bands of their altered minerals. For example, using Landsat-8 the iron-bearing (ferrous and ferric oxides) minerals are delineated using band ratios 4/5 and 6/5, whilst band ratio 6/7 is applied to detect high values of the hydroxyl-bearing minerals (kaolinite, alunite, muscovite, epidotes and chlorites) (*Gupta, 2003*).

Principal Component Analysis (PCA) is a commonly used enhancement technique in lithological and alteration mapping studies, mainly in metallogenetic areas (*Ruiz-Armenta and Prol-Ledesma, 1998*). The number of spectral bands input and the number of output principal components (PCs) are equal. Most of the data variability is captured by PC1, which also

identifies characteristics shared by all bands and frequently provides crucial structural information.

The vector of greatest pixel variance is represented by PC1. The second-highest variability is represented by PC2, which is orthogonal to PC1 and emphasizes the spectral differences between the visible and infrared bands. In comparison to the first two PCs, PC3 captures the third-largest variability, but the other PCs capture less variability (*Vincent, 1997; Gabr et al., 2010*).

3.2. Magnetic data

The aeromagnetic map, depicting total intensity is a part of the airborne magnetic, which was conducted by Aero-Service Division, Western Geophysical Company of America in 1984, for the Egyptian General Petroleum Corporation (EGPC) and the Egyptian Geological Survey and Mining Authority (EGSMA). This airborne survey was conducted along most of the Egyptian Eastern Desert. Following parallel flight lines are oriented in a NE–SW direction at 1.5 km spacing with an azimuth of $45°$ and $225°$ from the true north. Meanwhile, the tie lines were flown in a NW-SE direction at right angles to the main flight line direction with an azimuth of $135°$ and $315°$ from the true north (*Aero-Service, 1984*).

The reduced-to-pole (RTP) filter to rectify these data, the total main field value of 42425 nT was deducted from the overall intensity data using the International Geomagnetic Reference Field of 1980. The reduced-to-the-north magnetic pole (RTP) map of the research area was calculated using an inclination of $39.5°$ N and a declination of $2°$ E. This process is an essential step prior to applying any analytical technique, as the RTP centres the peaks of magnetic anomalies above their causative bodies (*Baranov, 1957*).

According to (*Philips, 1997*), the reduction-to-pole (RTP) is a technique in the frequency domain used to decrease the directional fuss that the low geomagnetic latitude caused. This technique is carried out on the gridded data that take off the asymmetry in total magnetic intensity (RMI) data that is caused by the non-vertical inclination of the Earth's magnetic field. The *Geosoft Oasis Montaj (2015)* software was used to compute RTP data in the spectrum domain as:

$$\text{La} = \frac{[\sin(\text{I}) - i \, \cos(\text{I}) \cos(\text{D} - \theta)]^2}{(\sin^2(\text{Ia}) + \cos^2(\text{Ia}) \cos^2(\text{D} - \theta)) \cdot (\sin^2(\text{I}) + \cos^2(\text{I}) \cos^2(\text{D} - \theta))} \, , \quad (1)$$

$$\text{if (Ia} \le \text{I), Ia} = \text{I} \, , \quad\quad\quad\quad\quad\quad\quad\quad\quad\quad\quad\quad\quad (2)$$

where the direction of the wavenumber vector in azimuth degrees = La, the inclination angle = I, the inclination for amplitude correction = Ia, and the declination angle = D. The RTP map serves as the primary dataset for any analytical or interpretative techniques.

Miller and Singh (1994) created the Tilt Angle filter to highlight features and identify the borders of causal bodies in potential field data. *Verduzco et al. (2004)* claimed that the tilt derivative filter also automatically detects anomalies in gain, which successfully draws attention to noticeable anomalies (*Cooper and Cowan, 2006*). The tilt angle produces zero value over the source edges, which is helpful in tracing them (*Miller and Singh, 1994*), which is the ratio of the vertical derivative to the absolute value of the horizontal derivative of the magnetic field:

$$\text{TDR} = \emptyset = \tan^{-1} \frac{\text{VDR}}{\text{THDR}} \, , \quad\quad\quad\quad\quad\quad\quad\quad\quad (3)$$

where, VDR = first vertical derivative, and THDR = total horizontal derivative.

On other hand, the CET Porphyry Detection system is used to locate and boundary the subcircular zonation type in the magnetic data related to the central intrusion and inner alteration zone of the porphyry system (*Holden et al., 2008; Macnae, 1995; Eldosouky et al., 2017*).

The CET system is composed of the following elements: (1) the Amplitude Contrast Transform to evaluate magnetic amplitude variations; (2) the Central Peak Detection to identify the centres of circular features; (3) the Circular Feature Transform to detect circular-shaped features (*Loy and Zelinsky, 2003*); and (4) Boundary Tracing to define the edges of the features (*Williams and Shah, 1990*).

At last, a semi-automatic process called Euler deconvolution (*Reid et al., 1990*) was submitted by *Thompson (1982)* to locate the depth of sources and evolved by *Reid et al. (1990)* to estimate the locations and the corresponding depth of geologic sources of magnetic or gravimetric anomalies in a two-dimensional grid.

Reid et al. (1990) automated the solution of the Euler linear equation of homogeneity for gridded data to produce solutions for the positions and depths of magnetic sources.

The usual Euler's equation is re-arranged in the form:

$$(x - x_0)\frac{\partial \mathrm{T}}{\partial x} + (y - y_0)\frac{\partial \mathrm{T}}{\partial y} + (z - z_0)\frac{\partial \mathrm{T}}{\partial z} + \mathrm{N}\left(\mathrm{B} - \mathrm{T}\right), \tag{4}$$

where, (x_0, y_0, z_0) is the position of a source whose total field T is detected at (x, y, z), B is the regional or the background of the total field, and N is the structural index (SI).

The Structural Index (SI) is an exponential factor corresponding to the rate at which the field falls off with distance from a source of a given geometry (*Reid et al., 1990*). The value of the SI parameter depends on the type of source body we are looking for and the type of potential field data we are using (magnetic or gravitational).

4. Results

4.1. Remote sensing results

In band ratio (BR), clay, mica, talc-carbonate, and carbonates, like marbles, are exemplification of hydroxyl minerals that show strong absorption in the 2.08–2.35 m wavelength region, which is identical to OLI-B7 (2.1–2.3 m). Additionally, the 1.55–1.75 m band, which corresponds to B6 (1.56–1.66 m) of Landsat-8, has a higher intensity of spectral reflectance.

Consequently, the best way to differentiate between carbonate minerals and hydroxyl-bearing changes is to use the 6/7 band ratio (Fig. 2a) (*Gupta, 2018; Pour and Hashim, 2015b*).

Ferrous (Fe^2) mafic minerals, such pyroxene and olivine, show high reflectance in B6 (1.560–1.660 m) and substantial absorption in OLI-B5 (0.845–0.885 m). Accordingly, gossans, ferrous-bearing rocks, and the distinction between mafic and felsic rocks may all be identified using the 6/5 band ratio (Fig. 2b) (*Zoheir et al., 2019a*).

In the visible and near-infrared (VNIR) spectrum, ferric (Fe^3) ions show a spectral response (*Gupta, 2018*). Iron oxide/hydroxide minerals, such as jarosite, hematite, and limonite, show significant absorption in the ultraviolet or blue spectral region (0.45–0.52 m), which corresponds to OLI-B2,

and intense reflectance in the near-red zone (0.63–0.69 m), corresponding to OLI-B4. According to *Pour and Hashim (2015b)*, this is what gives iron minerals their distinctive rusty reddish-brown hue. In order to highlight ferric-bearing iron minerals, the OLI-B4/2 band ratio (Fig. 2c). was used in this investigation (*Sabins, 1999*).
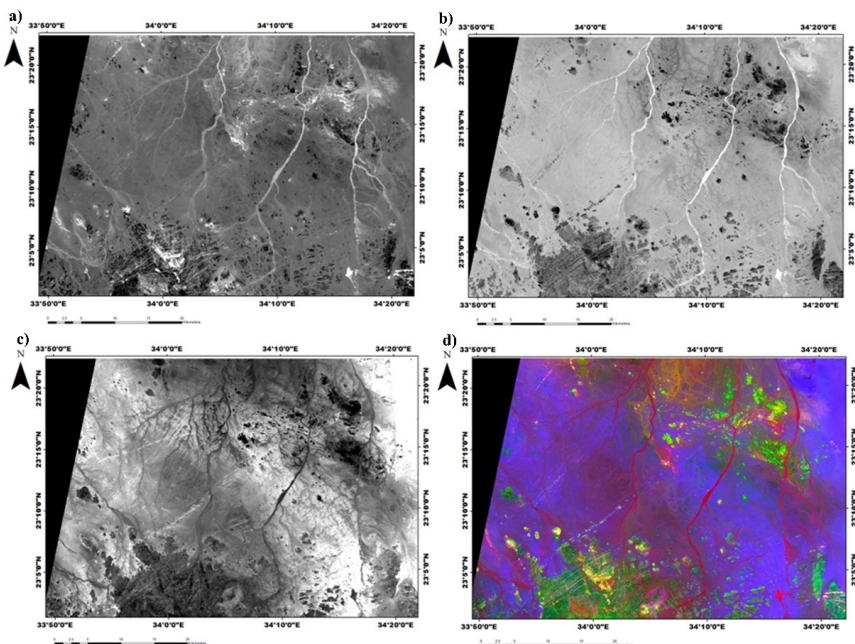

Fig. 2. a) BR of 6/7, highlighting the hydroxyl-bearing and carbonate alteration zones; b) BR of 6/5, sharpening the ferrous-bearing minerals; c) BR of 4/2, highlighting the ferric-bearing minerals; and d) false-colour composite image of BR: 6/7, 6/5, and 4/2 as RGB.

To highlight the combination of hydrothermal alteration minerals, a false-colour composite image was produced utilizing the band ratios 6/7, 6/5, and 4/2 as RGB (Fig. 2d). Light green highlights ferrous-bearing minerals, brilliant blue highlights ferric iron minerals, and light red, orange, pink, and yellowish hues emphasize hydroxyl minerals. Granites and metamorphic rocks are depicted in green due to their high iron oxide content. The mid-red hue associated with metasediments denotes a low concentration of silicate minerals and a high concentration of clay and iron minerals. Clay and ferric/ferrous oxide-rich alteration zones are indicated by areas high-

lighted in yellow.

Moreover, the Principal Components Analysis (PCA) or "Crósta" technique, which was applied to remote sensing data for mineral exploration (*Crósta et al., 2003*), the "Crósta" Method Target regions can be highlighted as either bright or dark pixels in principal component pictures produced using PCA (*Loughlin, 1991*). It is well-established that iron-bearing and clay minerals exhibit distinct absorption characteristics in specific bands. By applying PCA, maps of hydroxyl (OH)-bearing and iron-rich minerals can be extracted by transforming selected bands.

Four bands from Landsat 8 (bands 2, 5, 6, and 7) were chosen to identify regions rich in OH-bearing minerals (H-image) in order to map alteration zones (OH-bearing minerals) using the Crósta approach. To avoid mapping iron oxides, bands 2 and 3 were omitted (see Table 1; *Mia and Fujimitsu, 2012*). Subsidiary, the approach used by *Loughlin (1991)* and *Crósta et al. (2003)*, an evaluation of the eigenvector matrix's output was executed. The highest eigenvector properties, albeit with opposite values (+ or −), are usually found in the main component (PC) that retains the intended spectral information.

PC3 displays a considerable contrast between band 6 (0.999985) and band 7 (−0.003682) based on the PCA loading of the chosen bands (2, 5, 6, and 7) (Table 1). Because of this, PC3 successfully draws attention to the alteration zone, with affected rocks appearing significantly darker than other rock units (Table 1).

Thus, PC3 highlighted alteration zone in Compared to the other rock units, the altered rocks have a very dark tone (Table 1).

Table 1. PCA of the selected bands 2, 5, 6, and 7 of Landsat-8.

EIGENVECTOR	BAND2	BAND5	BAND6	BAND7	EIGENVALUE
PC1	0.999793	−0.019833	−0.003193	−0.003251	26082.437875
PC2	−0.019827	−0.999800	0.002486	−0.000542	618.401592
PC3	0.003230	0.002424	0.999985	−0.003682	63.307976
PC4	0.003251	−0.000598	0.003673	0.999988	13.413621

Additionally, the PCs used to identify regions rich in iron oxides were derived by transforming Landsat-8 bands 2, 4, 5, and 6 (Table 2). The findings indicate that PC3 aids in locating areas with a greater iron oxide

content by providing a good contrast between bands 5 (0.999934) and 6 (−0.007886) (Table 2). Therefore, PC3 is multiplied by −1 to get the F-image, which highlights regions of iron oxides (Table 2).

Table 2. PCA of the selected bands 2, 4, 5, and 6 of Landsat-8.

EIGENVECTOR	BAND2	BAND4	BAND5	BAND6	EIGENVALUE
PC1	0.999680	−0.022234	−0.007171	0.009652	26538.763333
PC2	−0.022178	−0.999741	0.004173	−0.002833	542.672099
PC3	0.007339	0.004034	0.999934	−0.007886	66.758719
PC4	0.009655	0.002586	0.007967	−0.999918	7.962649

The "Crósta alteration image" is a false-colour composite image created by using the OH-bearing minerals (H-image) in red (Fig. 3a), iron-bearing oxides (F-image) in blue (Fig. 3b), and the combined H+F image in green (Fig. 3c) after the H (hydroxyl-bearing) and F (iron oxide) images have been obtained in grayscale.

The alteration zones resulting from these combinations are clearly visible in (Fig. 3d). The reddish-yellow-highlighted false-colour composite image precisely depicts the distribution of OH-bearing minerals and iron oxides in the survey area.

The richer zones are shown in reddish-yellow (orange) in the final image, which delineates the alteration zones according to the abundance of iron oxides and OH-bearing minerals. Similar outcomes are seen in sedimentary rocks with high concentrations of clay minerals, particularly in the southwest quadrant and in certain alluvial sediments. Compared to the maps produced from band ratio alteration zones, the Crósta alteration image (Fig. 3d) offers a more distinct delineation of alteration zones in terms of number, size, area, and resolution.

Therefore, compared to the band ratio alteration zones map, the Crósta alteration picture for Gabal Abu Rahaya area proves to be more effective and potent for mapping alteration zones.

In the Eastern Desert of Egypt, mineralised zones are typically found close to or inside fracture networks. The transfer of hydrothermal fluids, which results in the creation of mineral deposits, is largely dependent on these lineaments and fracture systems. All rock units with different densities are intersected by linear features, so the lineaments Extraction, *O'Driscoll*

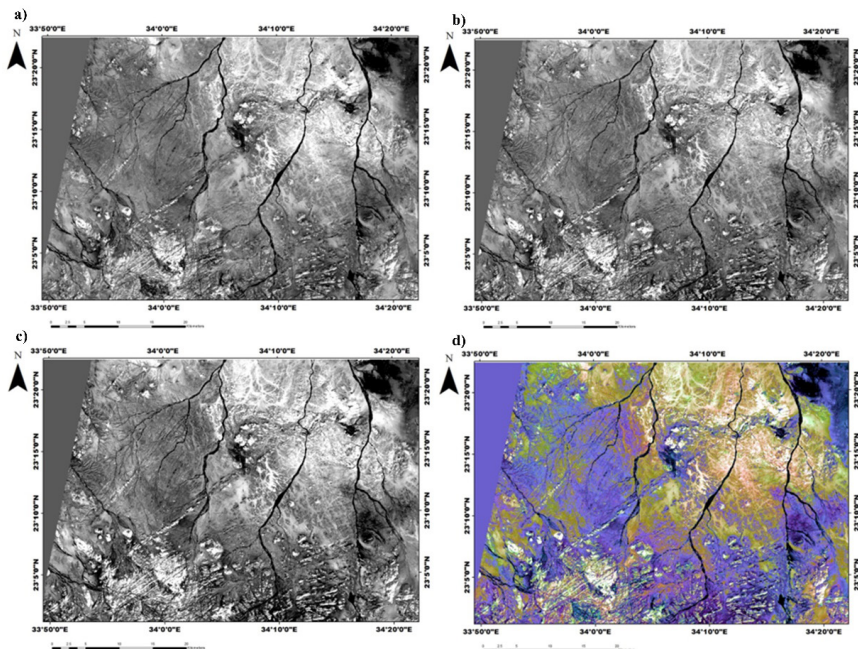*(1972)* asserts that lineaments can be used to locate possible mining re-
serves.

Fig. 3. a) False colour composite image using Crósta technique H-image; b) false colour
composite image using Crósta technique F-image; c) false colour composite image using
Crósta technique: (a) H-image F-image; and d) alteration areas in yellowish orange colour
after displaying h (R), F (B) and H+F (G).

This study traced several lithological units and extracted geological linea-
ments in the area of interest using data from the Shuttle Radar Topography
Mission (SRTM).

The research region is appropriate for this kind of investigation because
it is situated in an arid climate and has little vegetation. Lineament anal-
ysis was performed using Landsat-8 DEM data, and the main technique
for interpreting the SRTM DEMs was to create hill-shaded DEMs. In this
study, hill-shading DEMs with various azimuth angles and sun elevations
were used (Fig. 4a). This technique is effective in producing images that
enhance geomorphic lineaments.

Using azimuth and sun angle data, a grayscale DEM was used to create
the hill-shading image (Fig. 4b). Sun angles of less than $10°$ are extremely

dynamic in highlighting topography in low-relief areas, such as the study territory, and were therefore chosen for lineament analysis (*Peña and Abdesalam, 2006*). According to the findings, the shaded relief image offers insightful geological information. The structural inputs extracted from the SRTM DEM data are shown in the lineaments map (Fig. 4c) and the rose diagram depicting the orientation of the lineaments (Fig. 4d).
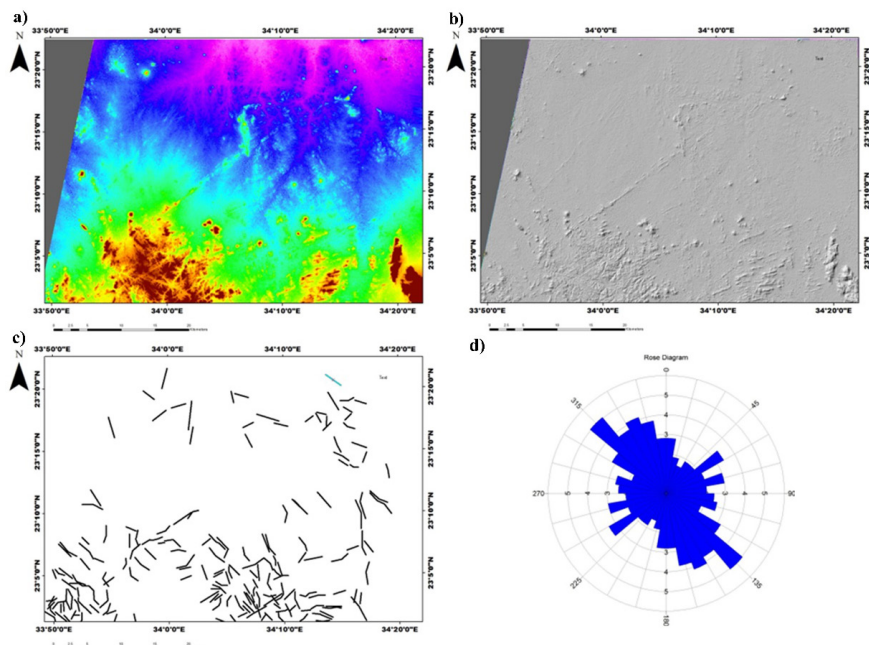

Fig. 4. a) Digital elevation model (DEM) of the study area: b) hill-shading image of the study area; c) lineaments map, extracted from the DEM of SRTM data; and d) rose diagram of lineaments extracted from surface remote sensing data.

Two primary fault systems may be identified in the tectonic trends within the research area based on the extracted lineaments map. The first system has numerous directional patterns and is linked to Precambrian tectonic activity: NNW–SSE to NW–SE, NE–SW, WNW–ESE, ENE–WSW, E–W, and N–S. The second system, which is mostly represented by NW–SE and NNE–SSW trends, evolved during the Phanerozoic epoch as a result of the Red Sea rifting process. The observed patterns coincide with the research of *Abdel Gawad (1967)* and are generally in line with earlier investigations conducted by *Hunting Geology and Geophysics (1967), Krs et al. (1973),*

and *Garson and Krs (1976)*. According to the data, the main N–S to NNW–SSE trends were formed during the Precambrian by a tectonic force that was roughly directed in an E–W direction. Secondary directions like ENE–WSW, WNW–ESE, NE–SW, NW–SE, and E–W were also present. During the Phanerozoic, stress oriented in the NNW–SSE direction led to the development of conjugate fault trends (NW–SE and NE–SW) and reactivated many of the older structures. The continuous development of the Red Sea rift is intimately related to these movements. In conclusion, the region's tectonic structure is a result of both more recent Phanerozoic tectonic pressures connected to Red Sea development and older Precambrian stresses.

4.2. Magnetic results

The magnetic method is widely recognised as a valuable and accessible tool for investigating both surface and subsurface geological structures. Aeromagnetic analysis is employed to address challenges related to regional geological mapping and structural interpretation (*Eldosouky, 2019; Sehsah et al., 2019; Eldosouky and Mohamed, 2021; Melouah and Pham, 2021*).

Aeromagnetic Interpretation Significant differences a qualitative elucidation of the Total Magnetic Intensity (TMI) map (Fig. 5a) reveals a range in magnetic intensity utility from -242.9 to 122.7 nT. These discrepancies are explained by alteration inside the lithology of the investigation region. Widespread magnetic anomalies with long wavelengths, weak magnetic responses, and low gradients are visible on the map. These irregularities, which have elongated and semi-circular shapes, are frequently linked to younger granitic formations in the southeast and metasedimentary rocks in the north.

On the other hand, the western region, which is covered by sedimentary rocks, and the southwestern and southeast regions' basement rocks exhibit stronger magnetic reactions.

The sources of these anomalies show trends in WNW–ESE to NW–SE, E–W, NE–SW, and N–S directions, suggesting that they are structurally aligned. The western, south-eastern, and north-eastern regions exhibit a maximum amplitude of roughly 245.092 nT.

The Reduced-to-Pole (RTP) magnetic anomaly map is presented at Fig. 5b. Both younger and older granites, as well as leucocratic metamor-
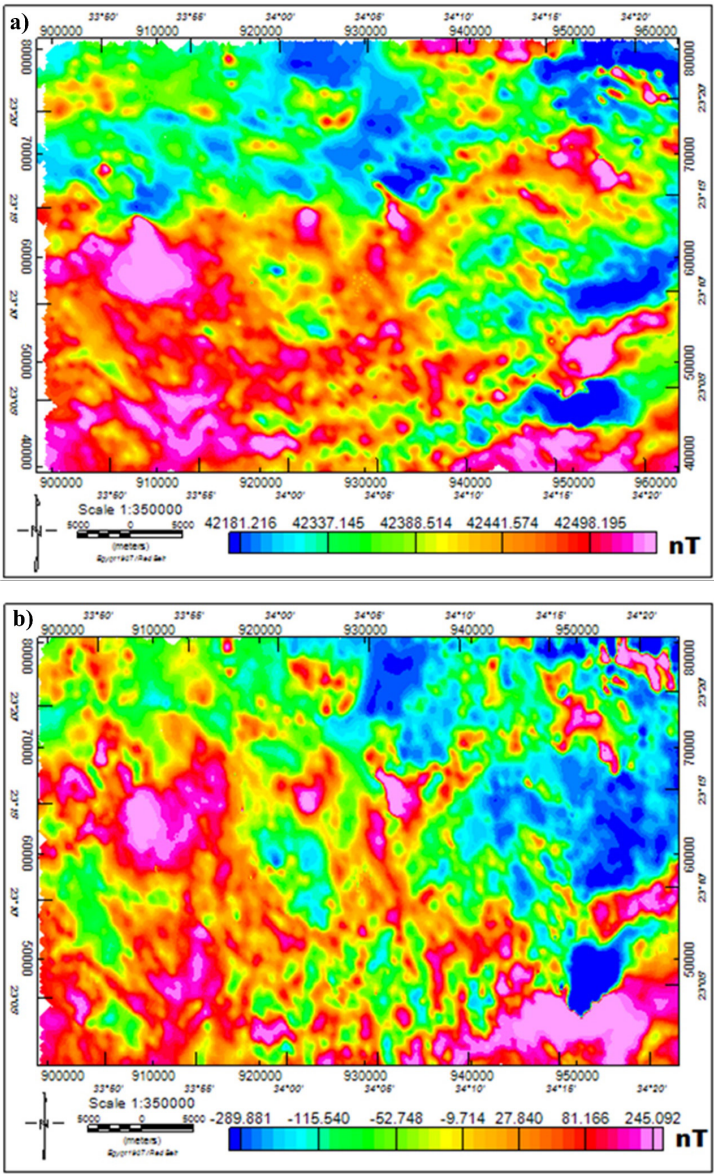
Fig. 5. a) Total magnetic intensity map; and b) RTP map of Gabal Abu Rahaya area.

phic rocks, are linked to these positive magnetic anomalies. While more widespread positive anomalies in the southern region trend toward the SW and WNW, the anomalies in the southeast and north-eastern regions are longer and directed in a NE direction.

Moreover, the north-eastern and southeast territory of the research area demonstrates mild magnetic anomalies correlated with metasediments and sedimentary rocks, running NE and SW directions, with a minimum amplitude of around -289.8815 nT.

Moreover, the RTP map (Fig. 5b) manifests that the plurality of magnetic anomalies parallel NW, SE, N–S, and E–W directions signalize the impact of regional tectonic processes such as the Syrian Arc system, the Red Sea, and the entrance of the Gulf of Suez.

Lineaments, which are interpreted as faults, are found using the Tilt Derivative (TDR) method, which makes it easier to locate extended magnetic source edges horizontally (*Miller and Singh, 1994*). The colour scale (Fig. 6) indicates that these lineaments are characterized by abrupt changes in magnetic susceptibility, especially at acute gradients where a faint yellow "zero-contour" line occurs between green (negative values) and red (positive values). According to the TDR data (Fig. 6) and extracted lineaments (Figs. 7a, 7b) the extracted structures coincide with the surface geology of basement rock which could host mineralisation that is consistent with the controlling NE–SW, NW–SE, and N–S trends. These trends are the main lineament trends in the study area.

Magnetic topography was clarified using the CET Porphyry analysis, which was first introduced by *Holden et al. (2011)* and was established on the methodology of *Macnae (1995)*.

The Reduced-to-Pole (RTP) magnetic data was subjected to this technique in four consecutive steps: boundary delineation, amplitude contrast transformation, central peak detection, and circular feature identification. The significance of circular features arises from the fact that intrusions, particularly porphyritic ones, generally have a circular or near-circular shape. The processes of mineralisation are often linked to these intrusions or occur in the surrounding areas due to the metamorphism of the host rock caused by the intrusion. Additionally, the intrusion creates fractures in the invaded rocks, providing a pathway for hydrothermal solutions, which facilitate mineralisation either through the direct emplacement of ores in these fractures
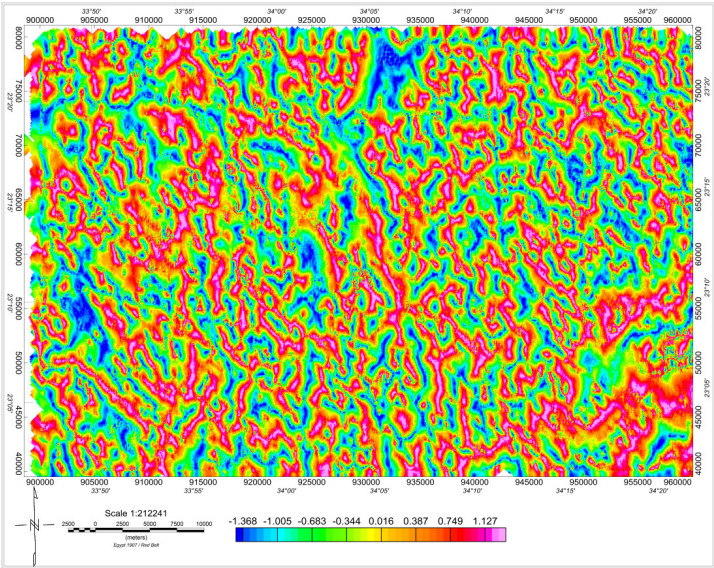
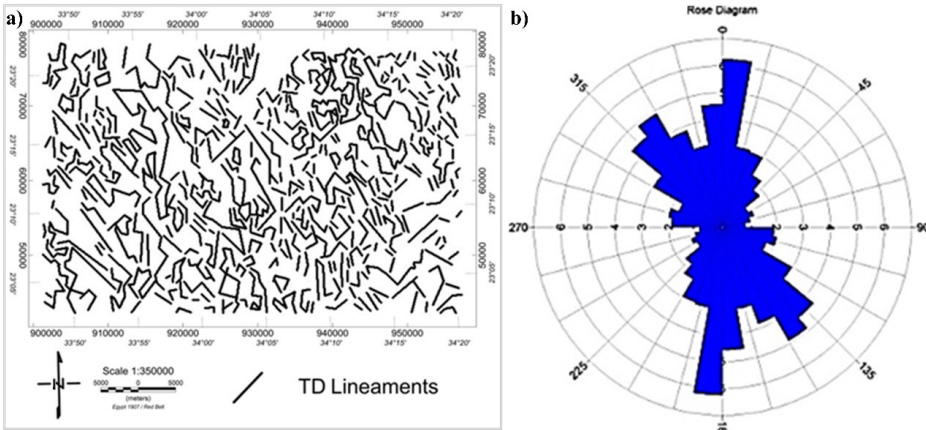Fig. 6. Tilt derivative map (in radians).

Fig. 7. Extracted lineaments from TDR; and b) rose diagram of TDR lineaments.

or through replacement processes (*Domzalski, 1964; Holden et al., 2011; Eldosouky et al., 2017*). The intrusions themselves have a positive magnetic polarity, whereas the surrounding alteration zones are much less magnetic,

which aids in the identification of these altered areas (*Holden et al., 2011; Eldosouky et al., 2017*). The CET porphyry intrusion maps displayed in Figs. 8 and 9 were produced as a result of these procedures.

The dyke-like features characteristics, which primarily align in NW–SE, NE–SW, and N–S directions, are structurally impacted, according to the analysis map (Fig. 8). This implies that the N–S structural trend is the result of the most recent tectonic activity, while the NW-oriented trend reflects the dominant and more established tectonic framework in the study area (*Eldosouky and Elkhateeb, 2018*) and these directions can be considered among the most favourable zones for mineralisation emplacement within the study area. It is worth noting that similar trends have been recorded in various parts of the south-eastern desert of Egypt and have been associated with known mineral deposits (*Ammar et al., 1983; El Rakaiby and Kamel, 1988; Hussein et al., 1988; Garson and Krs, 1976*, among others).

The areas of potential structural complexity shown in (Fig. 9) show the possible localities of mineralisation zones (marked as black triangles). These potential zones were superimposed to the map mineralisation occurrences in the study area (Fig. 10) to highlight and validate potential gold occurrences in these structural blocks of the ED of Egypt (*Zoheir et al., 2019a*).

The produced map from carrying out the standard Euler deconvolution technique to the RTP data (Fig. 11) shows a very good clustering of symbols in linear and curved style, showing the type of probable contacts between the rock units and showing the different geometries of the causative bodies, with the linear contacts proposed to be the result of faults, which means the contacts are structurally controlled. According to the results of the solution maps, the depths to the detected subsurface structures of the research region range from 0.2 to 1.2 km for dyke (SI = 1) with an average depth of 0.7 km. This range is typical of Euler analysis, which is often influenced by shallow subsurface sources.

Determining the depth to the top of the source is a valuable technique for estimating the thickness of sedimentary successions and, at times, for identifying key structural features within basement rocks. In sedimentary basin studies, it is generally assumed that erosional processes have reduced the vertical extent of intrusive rocks within the basement. Accordingly, the depth to the top of the intrusion represents the thickness of the overlying sedimentary section. However, this thickness is often considered a minimum
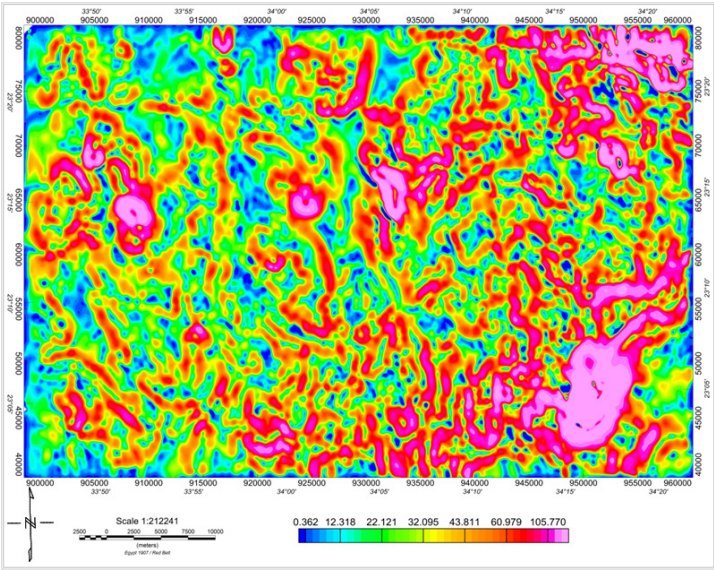
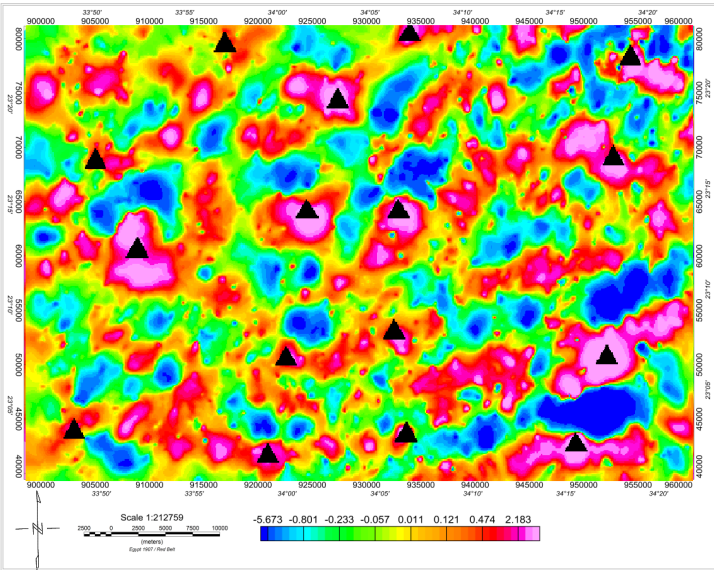Fig. 8. Amplitude contrast transform of the RTP.

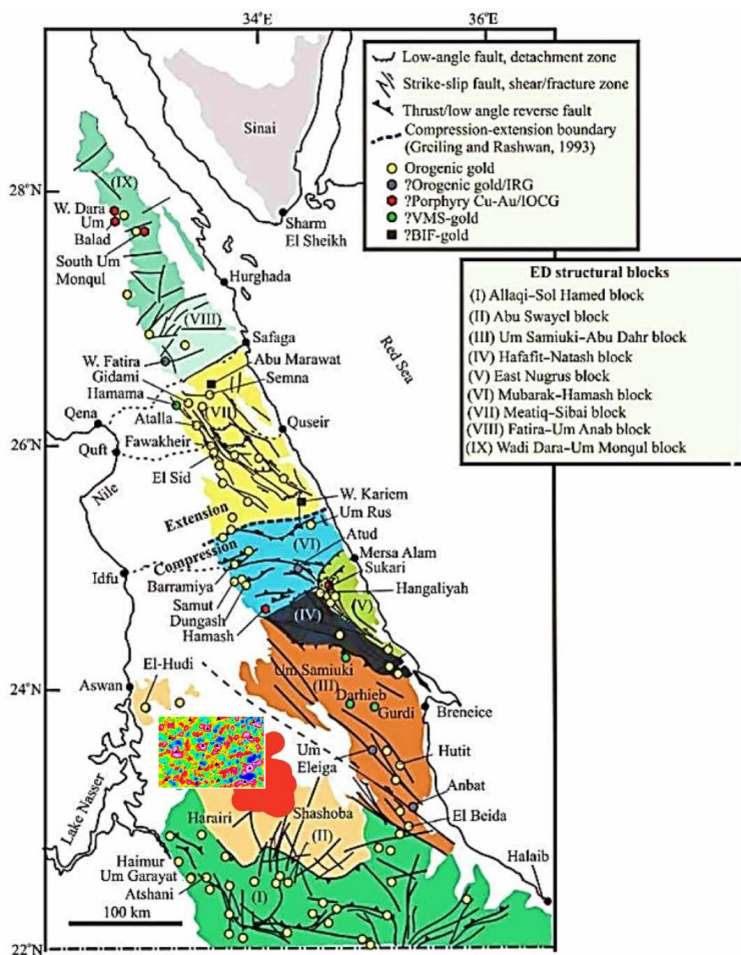Fig. 9. The porphyry detected features from boundary tracing.

382

Fig. 10. Opportunity map for mineralisation occurrences in the study area superimposed on the concentrations of gold occurrences in structural blocks of the ED of Egypt (*Zoheir et al., 2019a*) (small circles in the opportunity map are for known mineralisation sites).

estimate, as the intrusion may not extend all the way to the basement surface (*Dobrin, 1976*).

Basement depths (Fig. 12.) were calculated using standard Euler deconvolution with a structural index (SI) of 0.1. This data was used to construct a depth map of the magnetic sources across the study area. The map indicates that the greatest depths, exceeding 1 km, are found in the
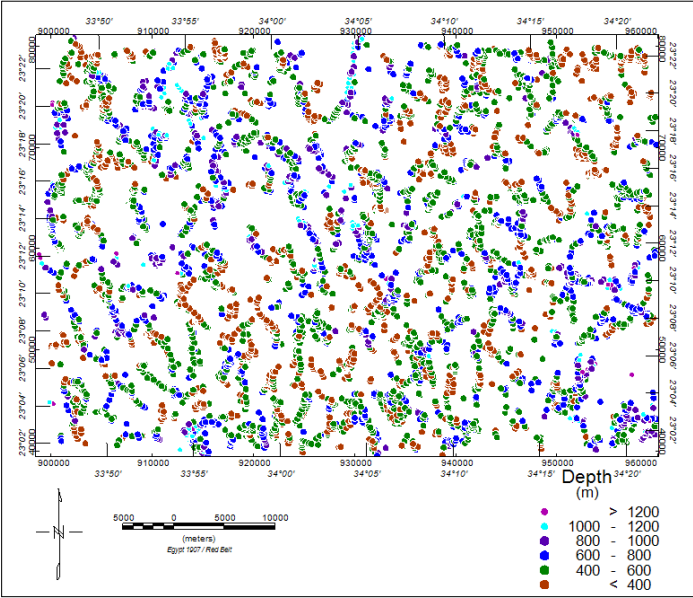
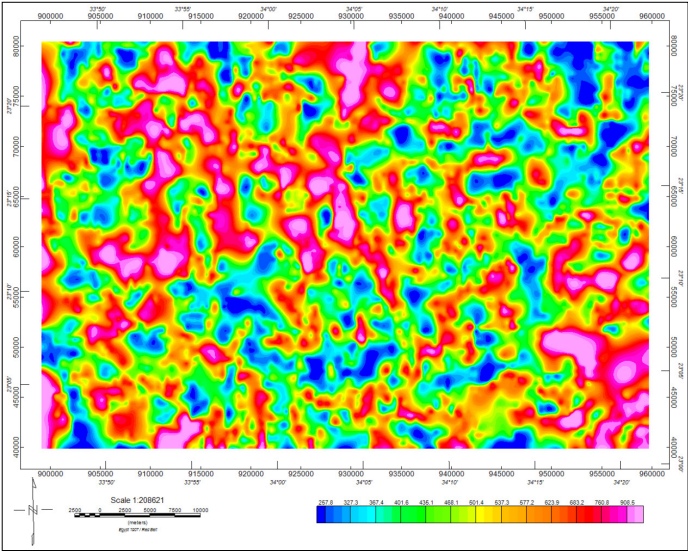Fig. 11. Standard Euler deconvolution applied to RTP with SI = 1.

Fig. 12. Depth map of causative sources conducted from Standard Euler deconvolution applied to RTP with SI = 1.

southwestern and north-eastern regions of the area, aligned with a NW–SE structural trend.

Figure 6 demonstrates a well-clustered distribution of solutions in both linear and curved patterns. These patterns reflect the interactions between different rock units and highlight the diverse geometries of the causative magnetic sources.

Furthermore, the TDR Euler and maps (Figs. 6 and 11) show strong alignment with circular features observed in the whole parts of the study area. These circular structures are considered highly favourable indicators for ore deposition, suggesting a strong potential for mineralisation in the region.

This correlation strongly supports the interpretation that lineaments commonly regarded as favourable zones for ore concentration coincide with the boundaries of subsurface magnetic sources. Additionally, the close spatial match between mineralised zones and circular features highlights the significant influence of structural systems on mineral accumulation processes, indicating that ore formation in the study area was largely controlled by tectonic structures.

5. Conclusion

The integrated results demonstrate the value of combining high-resolution aeromagnetic data with remote sensing techniques in identifying significant geological structures and areas with high mineral potential. The final mineral potential map provides a comprehensive interpretation of lithological, structural, and geophysical data, serving as a useful tool for guiding future exploration in the Gabal Abu Rahaya area. This combined approach enhances the understanding of regional geology and supports the development of more accurate and cost-effective mineral exploration strategies. The updated geological and mineral potential maps are essential references for ongoing and future geological and economic studies in Egypt's Eastern Desert. Moreover, the high number of detected sites, along with the fact that the area and its surroundings have had limited prior studies, underscores the need for more detailed future research.

Data availability. The data will be available on request from the corresponding author.

References

Aali A. A., Shirazy A., Shirazi A., Pour A. B., Hezarkhani A., Maghsoudi A., Hashim M., Khakmardan S., 2022: Fusion of remote sensing, magnetometric, and geological data to identify polymetallic mineral potential zones in Chakchak region, Yazd, Iran. Remote Sens., **14**, 23, 6018, doi: `0.3390/rs14236018`.

Abdel Gawad M., 1967: Geologic exploration and mapping from space. Presented at AAS Meeting, Boston, May 1967.

Abd El-Wahed M., Zoheir B., Pour A. B., Kamh S., 2021: Shear-related gold ores in the Wadi Hodein shear belt, South Eastern desert of Egypt: Analysis of remote sensing, field and structural data. Minerals, **11**, 5, 474, doi: `0.3390/min11050474`.

Abdel-Karim A.-A. M., 2021: Neoproterozoic Ophiolitic and Arc Metavolcanics of the Egyptian Nubian Shield. In: Hamimi Z., Arai S., Fowler A. R., El-Bialy M. Z. (Eds.): The Geology of the Egyptian Nubian Shield. Regional Geology Reviews. Springer, Cham, pp. 209–238, doi: `10.1007/978-3-030-49771-2_8`.

Abdelsalam M. G., Stern R. J., 1996: Sutures and shear zones in the Arabian-Nubian Shield. J. Afr. Earth Sci., **23**, 3, 289–310., doi: `0.1016/S0899-5362(97)00003-1`.

Aero-Service, 1984: Final operational report of airborne Magnetic/radiation Survey in the Eastern Desert, Egypt. Aeroservice for EGPC, Houston, Texas, April 1984, six volumes, an internal report, No. 3609.

Akaad M. K., El Ramly M. F., 1960: Geological history and classification of the basement rocks of the central Eastern desert of Egypt. Geol. Surv. Egypt, 9, 24 p.

Ammar A. A., Meleik M. L., Fouad K. M., 1983: Tectonic analysis of a sample area, Central Eastern Desert, Egypt, applying aero-radiometric and aeromagnetic survey data. Bull. Fac. Earth Sci., King Abdulaziz Univ., **6**, 459–482.

Banerjee K., Jain M. K., Jeyaseelan A. T., Panda S., 2019: Landsat 8 OLI data for identification of hydrothermal alteration zone in Singhbhum shear zone using successive band depth difference technique – a new image processing approach. Curr. Sci., **116**, 10, 1639–1647, doi: `0.18520/cs/v116/i10/1639-1647`.

Baranov V., 1957: A new method for interpretation of aeromagnetic maps: Pseudogravimetric anomalies. Geophysics, **22**, 2, 359–382, doi: `0.1190/1.1438369`.

Bencharef M. H., Eldosouky A. M., Zamzam S., Boubaya D., 2022: Polymetallic mineralization prospectivity modelling using multi-geospatial data in logistic regression: The Diapiric zone, Northeastern Algeria. Geocarto Int., **37**, 27, 15392–15427, doi: 0.1080/10106049.2022.2097481.

Cappaccioni B., Vaselli O., Moretti E., Tassi F., Franchi R., 2003: The origin of thermal water from the eastern flank of the Dead Rift Valley (western Jordan). Terra Nova, **15**, 3, 145–154, doi: 0.1046/j.1365-3121.2003.00476.x.

Chen G., Liang G., Xu D., Zeng Q., Fu S., Wei X., He Z., Fu G., 2004: Application of a shallow seismic reflection method to the exploration of a gold deposit. J. Geophys. Eng., **1**, 1, 12–16, doi: 0.1088/1742-2132/1/1/002.

Conoco, 1987: Geological Map of Egypt, scale 1:500,000, Sheet NF 36 NE-Berenice. The Egyptian General Petroleum Corporation (EGPC), Cairo, Egypt.

Cooper G. R. J., Cowan D. R., 2006: Enhancing potential field data using filters based on the local phase. Comput. Geosci., **32**, 10, 1585–1591, doi: 0.1016/j.cageo.2006.02.016.

Crósta A. P., De Souza Filho C. R., Azevedo F., Brodie C., 2003: Targeting key alteration minerals in epithermal deposits in Patagonia, Argentina, using ASTER imagery and principal component analysis. Int. J. Remote Sens., **24**, 21, 4233–4240, doi: 0.1080/0143116031000152291.

Dobrin M. B., 1976: Introduction to geophysical prospecting. McGraw-Hill Book Co., New York, USA, 630 p.

Domzalski W., 1964: Importance of aeromagnetic in evaluation of structural control of mineralization. Presented at the Twenty-fifth Meeting of the European Association of Exploration Geophysicists, Liège, June, 1964.

Ekwok S. E., Akpan A. E., Ebong E. D., 2019: Enhancement and modelling of aeromagnetic data of some inland basins, southeastern Nigeria. J. Afr. Earth Sci., **155**, 43–53, doi: 0.1016/j.jafrearsci.2019.02.030.

Eldosouky A. M., Abdelkareem M., Elkhateeb S. O., 2017: Integration of remote sensing and aeromagnetic data for mapping structural features and hydrothermal alteration zones in Wadi Allaqi area, South Eastern Desert of Egypt. J. Afr. Earth Sci., **130**, 28–37, doi: 0.1016/j.jafrearsci.2017.03.006.

Eldosouky A. M., Elkhateeb S. O., 2018: Texture analysis of aeromagnetic data for enhancing geologic features using co-occurrence matrices in Elallaqi area, South Eastern Desert of Egypt. NRIAG J. Astron. Geophys., **7**, 1, 155–161, doi: 0.1016/j.nrjag.2017.12.006.

Eldosouky A. M., 2019: Aeromagnetic data for mapping geologic contacts at Samr El-Qaa area, North Eastern Desert, Egypt. Arab. J. Geosci., **12**, 1, 2, doi: 0.1007/s12517-018-4182-2.

Eldosouky A. M., Sehsah H., Elkhateeb S. O., Pour A. B., 2020: Integrating aeromagnetic data and Landsat-8 imagery for detection of post- accretionary shear zones controlling hydrothermal alterations: The Allaqi-Heiani Suture zone, South Eastern Desert, Egypt. Adv. Space Res., **65**, 3, 1008–1024, doi: 0.1016/j.asr.2019.10.030.

Eldosouky A. M., Mohamed H., 2021: Edge detection of aeromagnetic data as effective tools for structural imaging at Shilman area, South Eastern Desert, Egypt. Arab. J. Geosci., **14**, 1, 13, doi: 0.1007/s12517-020-06251-4.

Eldosouky A. M., El-Qassas R. A. Y., Pour A. B., Mohamed H., Sekandari M., 2021: Integration of ASTER satellite imagery and 3D inversion of aeromagnetic data for deep mineral exploration. Adv. Space Res., **68**, 9, 3641–3662, doi: 0.1016/j.asr.2021.07.016.

Eldosouky A. M., Othman A., Saada A. S., Zamzam S., 2024: A New Vector for Mapping Gold Mineralization Potentialand Proposed Pathways in Highly Weathered BasementRocks using Multispectral, Radar, and Magnetic Datain Random Forest Algorithm. Nat. Resour. Res., **33**, 1, 23–50, doi: 0.1007/s11053-023-10292-3.

Elkhateeb S. O., Eldosouky A. M., 2016: Detection of porphyry intrusions using analytic signal (AS), Euler Deconvolution, and Center for Exploration Targeting (CET) Technique Porphyry Analysis at Wadi Allaqi Area, South Eastern Desert, Egypt. Int. J. Sci. Eng. Res., **7**, 6, 471–477.

El Rakaiby M. M. L., Kamel A. F., 1988: Factors controlling the distribution of radioactivity in south Eastern Desert, Egypt. Proc. 4th Conference on Nuclear Science and Applications, **1**, pp. 186–192.

Elsayed Zeinelabdein K. A., El-Nadi A. H. H., Babiker I. S., 2020: Prospecting for gold mineralization with the use of remote sensing and GIS technology in North Kordofan state, central Sudan. Sci. Afr., **10**, e00627, doi: 0.1016/j.sciaf.2020.e00627.

El-Shimi K. A., 2005: Application of remote sensing in mineral exploration at Wadi Allaqi district, SW-Eastern Desert of Egypt. Ann. Geol. Surv. Egypt, **XXVIII**, 205–223.

El Tarras M. M., 1995: Photogeologic, radiometric and magnetic studies of Gabel Diheisa – Gabel Tarbtie area, Southeastern Desert, Egypt. M.Sc. Thesis, Faculty of Science, Tanta University.

Gabr S., Ghulam A., Kusky T., 2010: Detecting areas of high-potential gold mineralization using ASTER data. Ore Geol. Rev., **38**, 1-2, 59–69, doi: 0.1016/j.oregeorev.2010.05.007.

Garson M. S., Krs M., 1976: Geophysical and geological evidence of the relationship of Red Sea transverse tectonics to ancient features. Geol. Soc. Am. Bull., **87**, 2, 169–181, doi: 0.1130/0016-7606(1976)87<169:GAGEOT>2.0.CO;2.

Geosoft Oasis Montaj, 2015: Data processing and analysis systems for Earth science applications (ver. 8.3.3). Geosoft Inc., Toronto.

Gerck E., Hurtak J. J., 1992: Laser remote sensing of forest and crops in genetic-rich tropical areas. International Archives of Photogrammetry and Remote Sensing. Proc. XVIIth ISPRS Congress, Washington DC, **XXIX**, B7, Comm. VII., pp. 436–438.

Gupta R. P., 2003: Remote Sensing Geology (2nd ed.). Springer Berlin, Heidelberg, Germany, 656 p.

Gupta R. P., 2018: Remote Sensing Geology (3rd ed.). Springer-Verlag, Berlin Heidelberg, Germany.

Haldar S. K., 2018: Mineral Exploration: Principles and Applications. Elsevier, Amsterdam, 378 p.

Holden E.-J., Dentith M., Kovesi P., 2008: Towards the automatic analysis of regional aeromagnetic data to identify regions prospective for gold deposits. Comput. Geosci., **34**, 11, 1505–1513, `doi: 0.1016/j.cageo.2007.08.007`.

Holden E.-J., Fu C. S., Kovesi P., Dentith M., Bourne B., Hope M., 2011: Automatic identification of responses from porphyry intrusive systems within magnetic data using image analysis. J. Appl. Geophys., **74**, 4, 255–262, `doi: 0.1016/j.jappgeo.2011.06.016`.

Howari F. M., Ghrefat H., Nazzal Y., Galmed M. A., Abdelghany O., Fowler A. R., Sharma M., AlAydaroos F., Xavier C. M., 2020: Delineation of copper mineralization zones at Wadi Ham, Northern Oman mountains, United Arab Emirates using multispectral Landsat 8 (OLI) data. Front. Earth Sci., **8**, 578075, `doi: 0.3389/feart.2020.578075`.

Hunting Geology and Geophysics Ltd., 1967: Assessment of the Mineral Potential of the Aswan Region. United Nations Development Program, Internal Report, 138 p.

Hussein H. A., Mansour S. L., Kamel A. F., El-Reedy M. W., 1988: Distribution of radioactivity in Um Deweila dyke, southern desert Egypt. Proc. 4th Conference on Nuclear Science and Applications, 1, 156–163.

Khalifa A., Bashir B., Çakir Z., Kaya Ş., Alsalman A., Henaish A., 2021: Paradigm of geological mapping of the Adiyaman fault zone of Eastern Turkey using Landsat 8 remotely sensed data coupled with PCA, ICA, and MNFA techniques. ISPRS Int. J. Geo-Inf., **10**, 6, 368, `doi: 0.3390/ijgi10060368`.

Kharbish S., Eldosouky A. M., Amer O., 2022: Integrating mineralogy, geochemistry and aeromagnetic data for detecting Fe–Ti ore deposits bearing layered mafic intrusion, Akab El-Negum, Eastern Desert, Egypt. Sci. Rep., **12**, 15474, `doi: 0.1038/s41598-022-19760-x`.

Krs M., Soliman A. A., Amin A. H., 1973: Geophysical phenomena over deep-seated tectonic zones in the southern part of Eastern Desert of Egypt. Ann. Geol. Surv. Egypt, **2**, 125–138.

Kusky T. M., Ramadan T. M., 2002: Structural controls on Neoproterozoic mineralization in the South Eastern Desert, Egypt: An integrated field, Landsat TM, and SIR-C/X SAR approach. J. Afr. Earth Sci., **35**, 1, 107–121, `doi: 0.1016/S0899-5362(02)00029-5`.

Loughlin W. P., 1991: Principal component analysis for alteration mapping. Photogramm. Eng. Remote Sens., **57**, 9, 1163–1169.

Loy G., Zelinsky A., 2003: Fast radial symmetry for detecting points of interest. IEEE Trans. Pattern Anal. Mach. Intell., **25**, 8, 959–973, `doi: 0.1109/TPAMI.2003.1217601`.

Macnae J., 1995: Applications of geophysics for the detection and exploration of kimberlites and lamproites. In: Griffin W. L. (Ed.): Diamond Exploration into the 21st Century. J. Geochem. Explor., **53**, 1-3, 213–243, `doi: 0.1016/0375-6742(94)00057-I`.

Mahdi A. M., Eldosouky A. M., El Khateeb S. O., Youssef A. M., Saad A. A., 2022: Integration of remote sensing and geophysical data for the extraction of hydrothermal al-

teration zones and lineaments; Gabal Shilman basement area, Southeastern Desert, Egypt. J. Afr. Earth Sci., **194**, 104640, `doi: 0.1016/j.jafrearsci.2022.104640`.

Mahmoud M. S., Essa M. A., 2007: Palynology of some Cretaceous mudstones from southeast Aswan, Egypt: significance to regional stratigraphy. J. Afr. Earth Sci., **47**, 1, 1–8, `doi: 0.1016/j.jafrearsci.2006.10.002`.

Maleki M., Niroomand S., Rajabpour S., Pour A. B., Ebrahimpour S., 2022: Targeting local orogenic gold mineralisation zones using data-driven evidential belief functions: The Godarsorkh area, Central Iran. All Earth, **34**, 1, 259–278, `doi: 10.10 80/27669645.2022.2129132`.

Melouah O., Pham L. T., 2021: An improved ILTHG method for edge enhancement of geological structures: application to gravity data from the Oued Righ valley. J. Afr. Earth Sci., **177**, 104162, `doi: 0.1016/j.jafrearsci.2021.104162`.

Mia B., Fujimitsu Y., 2012: Mapping hydrothermal altered mineral deposits using Landsat 7 ETM+ image in and around Kuju volcano, Kyushu, Japan. J. Earth Syst. Sci., **121**, 4, 1049–1057, `doi: 0.1007/s12040-012-0211-9`.

Miller H. G., Singh V., 1994: Potential field tilt—a new concept for location of potential field sources. J. Appl. Geophys., **32**, 2-3, 213–217, `doi: 0.1016/0926-9851(94)900 22-1`.

O'Conner E. A., Bennett J. D., Rashwan A. A., Nasr B. B., Mansour M. M., Romani R. F., Sadek M. F., 1994: Crustal growth in the Nubian Shield of south Eastern Desert, Egypt. Proc. Int. Conf. 30 years Cooper, Geol. Surv. Egypt Spec. Pub., **69**, pp. 189–195.

O'Driscoll K., 1972: Impact of active management on delivery unit practice. Proc. R. Soc. Med., **65**, 8, 697–698, `doi: 0.1177/003591577206500815`.

Peña S. A., Abdesalam M. G., 2006: Orbital remote sensing for geological mapping in southern Tunisia: Implication for oil and gas exploration. J. Afr. Earth Sci., **44**, 2, 203–219, `doi: 0.1016/j.jafrearsci.2005.10.011`.

Phillips J. D., 1997: Potential-field geophysical software for the PC, version 2.2: U.S. Geol. Surv., Open-File Report 97-725, 34 p., `doi: 0.3133/ofr97725`.

Pour A. B., Hashim M., 2015a: Integrating PALSAR and ASTER data for mineral deposits exploration in tropical environments: a case study from central belt, Peninsular Malaysia. Int. J. Image Data Fusion, **6**, 2, 170–188, `doi: 0.1080/19479832.20 14.985619`.

Pour A. B., Hashim M., 2015b: Structural mapping using PALSAR data in the Central Gold Belt, Peninsular Malaysia. Ore Geol. Rev., **64**, 13–22, `doi: 0.1016/j.oregeo rev.2014.06.011`.

Pour A. B., Hashim M., Makoundi C., Zaw K., 2016: Structural mapping of the Bentong-Raub suture zone using PALSAR remote sensing data, Peninsular Malaysia: Implications for sediment-hosted/orogenic gold mineral systems exploration. Resour. Geol., **66**, 4, 368–385, `doi: 0.1111/rge.12105`.

Pour A. B., Park T.-Y. S., Park Y., Hong J. K., Zoheir B., Pradhan B., Ayoobi I., Hashim M., 2018: Application of multi-sensor satellite data for exploration of Zn–Pb sulfide mineralization in the Franklinian basin, North Greenland. Remote Sens., **10**, 8, 1186, `doi: 0.3390/rs10081186`.

Pour A. B., Zoheir B., Pradhan B., Hashim M., 2021: Editorial for the special issue: Multispectral and hyperspectral remote sensing data for mineral exploration and environmental monitoring of mined areas. Remote Sens., **13**, 3, 519, `doi: 0.3390/rs13030 519`.

Reid A. B., Allsop J. M., Granser H., Millett A. J., Somerton I. W., 1990: Magnetic interpretation in three dimensions using Euler deconvolution. Geophysics, **55**, 1, 80–91, `doi: 0.1190/1.1442774`.

Ruiz-Armenta J. R., Prol-Ledesma R. M., 1998: Techniques for enhancing the spectral response of hydrothermal alteration minerals in Thematic Mapper images of Central Mexico. Int. J. Remote Sens., **19**, 10, 1981–2000, `doi: 0.1080/014311698215108`.

Sabins F. F., 1997: Remote Sensing; Principles and Interpretation (3rd ed.). New York: W. H. Freeman and Co., 499 p.

Sabins F. F., 1999: Remote sensing for mineral exploration. Ore Geol. Rev., **14**, 3-4, 157–183, `doi: 0.1016/S0169-1368(99)00007-4`.

Sehsah H., Eldosouky A. M., El Afandy A. H., 2019: Unpaired ophiolite belts in the Neoproterozoic Allaqi-Heiani Suture, the Arabian-Nubian Shield: Evidences from magnetic data. J. Afr. Earth Sci., **156**, 26–34, `doi: 0.1016/j.jafrearsci.2019.05.002`.

Sekandari M., Masoumi I., Pour A. B., Muslim A. M., Hossain M. S., Misra A., 2022: ASTER and WorldView-3 satellite data for mapping lithology and alteration minerals associated with Pb-Zn mineralization. Geocarto Int., **37**, 6, 1782– 1812, `doi: 0.1080/10106049.2020.1790676`.

Stern R. J., 1994: Arc assembly and continental collision in the Neoproterozoic East African Orogen: Implications for the consolidation of Gondwanaland. Annu. Rev. Earth Planet. Sci., **22**, 319–357, `doi: 0.1146/annurev.ea.22.050194.001535`.

Thompson D. T., 1982: EULDPH: A new technique for making computer-assisted depth estimates from magnetic data. Geophysics, **47**, 1, 31–37, `doi: 0.1190/1.1441278`.

Verduzco B., Fairhead J. D., Green C. M., MacKenzie C., 2004: New insights into magnetic derivatives for structural mapping. Lead. Edge, **23**, 2, 116–119, `doi: 0.1190/ 1.1651454`.

Vincent R. K., 1997: Fundamentals of Geological and Environmental Remote Sensing. Prentice Hall Series in Geographic Information Science. xiii + 370 p., Hemel Hempstead: Prentice Hall.

Weissbrod T., Karcz I., Abed A., 1988: Discussion on the supposed Precambrian palaeosuture along the Dead Sea Rift. J. Geol. Soc., **145**, 3, 515–517, `doi: 0.1144/gsjgs.14 5.3.0515`.

Williams D. J., Shah M., 1990: Edge contours using multiple scales. Comput. Gr. Image Process., **51**, 3, 256–274, `doi: 0.1016/0734-189X(90)90003-E`.

Zoheir B., Emam A., El-Amawy M., Abu-Alam T., 2018: Auriferous shear zones in the central Allaqi–Heiani belt: Orogenic gold in post-accretionary structures. SE Egypt. J. Afr. Earth Sci., **146**, 118–131, `doi: 0.1016/j.jafrearsci.2017.10.017`.

Zoheir B., Abd El-Wahed M., Pour A. B., Abdelnasser A., 2019a: Orogenic Gold in Transpression and Transtension Zones: Field and Remote Sensing Studies of the Barramiya–Mueilha Sector, Egypt. Remote Sens., **11**, 18, 2122, `doi: 0.3390/rs1118 2122`.

Zoheir B., Emam A., Abd El-Wahed M., Soliman N., 2019b: Gold endowment in the evolution of the Allaqi-Heiani suture, Egypt: A synthesis of geological, structural, and space-borne imagery data. Ore Geol. Rev., **110**, 102938, `doi: 0.1016/j.oregeorev.2019.102938`.

Zoheir B. A., Johnson P. R., Goldfarb R. J., Klemm D. D., 2019c: Orogenic gold in the Egyptian Eastern Desert: Widespread gold mineralization in the late stages of Neoproterozoic orogeny. Gondwana Res., **75**, 184–217, `doi: 0.1016/j.gr.2019.06.002`.